Periodic magnetic domains in single-crystalline cobalt filament arrays

Fei Chen, Fan Wang, Fei Jia, Jingning Li, Kai Liu, Sunxiang Huang, Zhongzhi Luan, Di Wu, Yanbin Chen, Jianmin Zhu, Ru-Wen Peng, and Mu Wang

Phys. Rev. B **93**, 054405 — Published 3 February 2016

DOI: 10.1103/PhysRevB.93.054405

Periodic Magnetic Domains in Single-Crystalline Cobalt Filament Arrays

Fei Chen,[1] Fan Wang,[1] Fei Jia,[1] Jingning Li,[1] Kai Liu,[2] Sunxiang Huang,[3] Zhongzhi Luan,[1] Di Wu,[1] Yanbin Chen,[1] Jianmin Zhu,[1] Ru-Wen Peng,[1] and Mu Wang[1,*]

[1] *National Laboratory of Solid State Microstructures, School of Physics, and Collaborative Innovation Center of Advanced Microstructures, Nanjing University, Nanjing 210093, China*
[2] *Department of Physics, University of California, Davis, CA 95616, USA*
[3] *Department of Physics, University of Miami, Coral Gables, FL 33146, USA*

(Dated: January 15, 2016)

Magnetic structures with controlled domain wall pattern may be applied as potential building blocks for three-dimensional magnetic memory and logic devices. Using a unique electrochemical self-assembly method, we achieve regular single-crystalline cobalt filament arrays with specific geometric profile and crystallographic orientation, and the magnetic domain configuration can be conveniently tailored. We report for the first time the transition of periodic anti-parallel magnetic domains to a compressed vortex magnetic domains depending on the ratio of height vs. width of the wires. A "phase diagram" is obtained to describe the dependence of the type of magnetic domains and the geometrical profiles of the wires. Magnetoresistance of the filaments demonstrates that the contribution of series of 180^o domain walls is over 0.15% of the zero-field resistance $\rho(H = 0)$. These self-assembled magnetic nanofilaments, with controlled periodic domain patterns, offer an interesting platform to explore domain-wall-based memory and logic devices.

PACS numbers: 75.60.Ch, 75.70.Kw, 75.75.-c, 82.45.Qr

I. INTRODUCTION

An efficient, reliable and non-dissipative way of information transmission and storage is essential in modern information technology, where heat dissipation problem has in fact become one of the major obstacles to further increasing the density and operation speed of integrated circuits.[1] Using electron spin as an alternative state variable,[2,3] instead of electric charge, the heat dissipation in nanoelectronics is expected to be substantially reduced.[4] As an example, magnetic domain walls (DWs) have been prominently featured in race-track memory[5,6] as well as magnetic logic devices,[7] where the spin-transfer or spin-orbit torque is utilized to manipulate DWs.[6,8–11] Recent advances in chiral DWs have led to the exciting possibility of using the topological feature of spin textures for information storage.[12–15] Integration of DW arrays with perpendicular anisotropy systems have also been proposed for three-dimensional (3D) spintronic memory and logic.[11,16] There have indeed been keen interests in achieving 3D magnetic nanostructures as building blocks for these envisioned devices,[17,18] which are challenging for nowadays fabrication approaches.

On the other hand, to control the magnetic domain and DW configurations in nanostructures, it is important to tailor the magneto-crystalline, shape and other anisotropies ,[19–22] which sensitively depend on crystalline orientation, size, shape and edge details of the sample.[23–25] By tuning the magneto-crystalline and shape anisotropy, the spatial configuration of the magnetic moments can be tuned, which is highly desirable for device applications.[26–31] Periodic magnetic domain pattern on nano-stripes made by micro-lithography has indeed been studied.[32–34] However, it remains challenging to tune the competition between magneto-crystalline and shape anisotropy in a convenient and cost-effective way,[20,35–37] which adds another layer of complexity to lithographical patterning of magnetic nanostructures.

In this work we report a self-assembly approach to achieve single-crystalline cobalt nano filaments with controlled size, shape and crystallographic orientation, which may be applied as potential building blocks for designing 3D DW-based magnetic memory and logic devices. The filaments have smooth surfaces with a flat cross-section resembling half of a ellipse. A "phase diagram" of the magnetic domain pattern and the geometrical parameters of the filaments is obtained. When the aspect ratio of the filament cross-section σ (defined as the ratio of height vs. width) is small, anti-parallel magnetic domain configuration emerges, and the state is robust against demagnetization; for larger σ value, a compressed vortex domain pattern appears. Periodic antiparallel magnetic domain pattern on entire filament array can be realized at remanence after applying a saturation magnetic field perpendicular to the plane of the filament arrays. This feature is attractive for potential applications in DW-based devices. Such configurations also allow us to identify the contribution of the domain walls on magneto-resistance (MR). The last but not the least, we should emphasize that this fabrication approach is essentially an electrochemical method, it is not restricted to the fabrication of cobalt filaments only. It can be applied to grow the nano-filament arrays of other magnetic metals and even alloys.[38]

II. EXPERIMENTALS

Sample fabrication was carried out in the electrochemical deposition cell, where 40 μL of electrolyte solution

of $CoSO_4$ (initial concentration 0.01 M and pH∼2.5) was sandwiched by a polished silicon substrate and a cover glass plate. Two cobalt wires (diameter 0.1 mm, 99.995% pure) were used as electrodes, and were placed in parallel with a separation of 5 mm. A Peltier element (size:$23 \times 23 \times 3.7mm^3$, maximum power:14.7 W) was placed underneath the silicon wafer in order to quickly adjust the temperature of the system. The entire setup was sealed in a copper chamber cooled by a thermostat, similar to that reported earlier.[39–45] The temperature of the thermostat could be controlled between −20°C to 100°C with accuracy of 0.01°C (Cole-Parmer, WX-12101-55, with 50% glycol and 50% deionized water as the circulating fluid). An optical microscope was applied to monitor the freezing and melting process of the electrolyte, and the electrochemical deposition process could be observed *in situ* as well. In the experiment the temperature of the thermostat was set to −1°C, and an electric voltage was applied on the Peltier element to freeze the electrolyte. Thereafter, by alternating switching the poles of the Peltier element, freezing-melting processes occurred alternatively. By carefully control of such process, eventually only one nucleus of the electrolyte ice was left in the system. The solidification rate was then controlled by decreasing temperature slowly using the thermostat (usually at −1.3°C). Finally a flat, uniform single-crystalline ice of electrolyte was formed. When the equilibrium was eventually reached, an ultrathin electrolyte was trapped in between the ice and the substrates due to the partitioning effect in the solidification process.[43,46] The thickness of this ultrathin electrolyte layer is on the order of 200nm, which depended on the temperature and the initial concentration of electrolyte.[42] In our electrodeposition process a potentiostatic voltage of 1.5 V was applied across the electrodes. The cobalt filaments initiated from the cathode and grew towards the anode in the ultrathin electrolyte layer trapped between the ice and the substrate. When the growth was finished, the electrodeposits on the substrate were then rinsed thoroughly with deionized water, dried and stored in a vacuum tank for characterization.

The topography of the cobalt arrays was observed with a field-emission scanning electron microscope (LEO 1530VP SEM) with InLens mode. The structure of cobalt filaments was analyzed by a transmission electron microscope (FEI TEM, Tecnai F20). Atomic force microscopy (AFM, Digital Instruments, Nanoscope IIIa) with magnetic force microscopy (MFM) mode, sensitive to out-of-plane stray field, was applied to characterize both the topography and the magnetic domains of the filaments, respectively. The demagnetization process was accomplished with a homemade Helmholtz coil with a maximum homogeneous magnetic field of 0.6T. Micromagnetic simulations were carried out with the OOMMF code.[47] The geometrical parameters of the filament in simulation was based on AFM measurements. For cobalt filament, the material parameters were selected as follows: saturation magnetization $M_s = 1.4 \times 10^6 A/m$, exchange stiffness $A_{ex} = 2.3 \times 10^{-11} J/m$, and uniaxial anisotropy constant $K_u = 4.0 \times 10^5 J/m^3$ in-plane and orthogonal to the filament. The cell size was set as $5 \times 5 \times 5nm^3$ (smaller than the exchange length of *hcp* cobalt, which is estimated as 7nm[48]) and the dimensionless damping was chosen as 0.5. MR measurements of the filaments were carried out by standard four-probe configuration with Au micro-electrodes fabricated by photolithography, and the external magnetic field was applied with the homemade Helmholtz coil.

III. RESULTS AND DISCUSSION

The arrays of electrodeposited cobalt filaments examined by an optical microscope are shown in Fig. 1(a), where the filaments are smooth and nearly parallel. Note that the brightness of the filament varies slightly at different locations due to spatial variation of the geometrical profile of filament. SEM micrograph of the cobalt filaments shows that the width of the filaments is not always uniform, and the broader regions have rougher edges with some branch-like features, as marked by the arrow in Fig. 1(b).

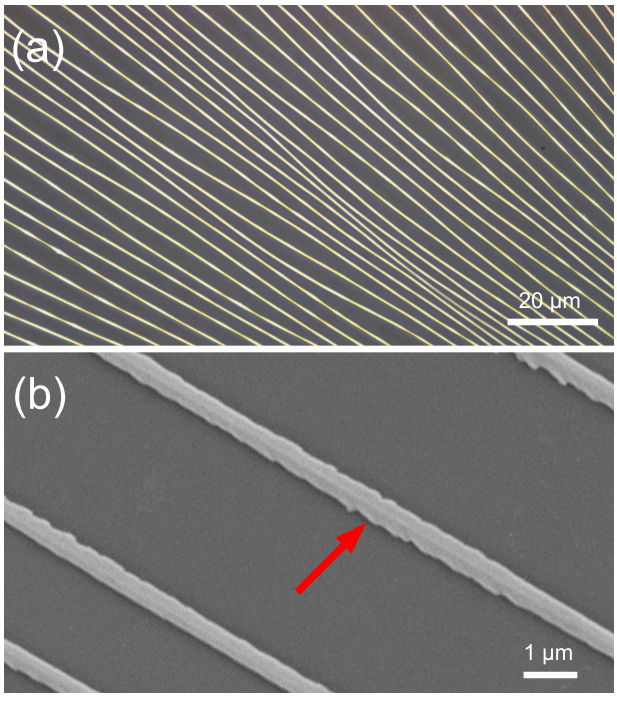

FIG. 1. (a) Optical micrograph of the cobalt filaments arrays, showing smooth and unbranched filaments. (b) SEM micrograph of the filaments. In some places the edge of the filament is rough, with some underdeveloped sidebranches, as marked by the arrow.

A TEM micrograph of the filament is shown in Fig. 2(a). Electron diffraction patterns of the selected sites [circles in Fig. 2(a)] indicate that the filament is a well-aligned single crystal and possesses *hcp* structure

[Figs. 2(b)-2(e)]. Note that the cobalt filament has been bent slightly during sample preparation. Accordingly the diffraction patterns at different sites along the filament are slightly rotated. The preferred growth direction of the filament is $< 11\bar{2}0 >$. The other equivalent preferred growth directions, such as $< 1\bar{2}10 >$ and $< \bar{2}110 >$, do not exist in-plane. In our ultra-thin electrolyte layer system the growth along those directions is consequently suppressed, while $< 11\bar{2}0 >$ becomes the only preferred growth direction. Note that the easy magnetization direction of cobalt,[24] $< 0001 >$, is perpendicular to the long axis of the filament, which is a key feature in our samples.

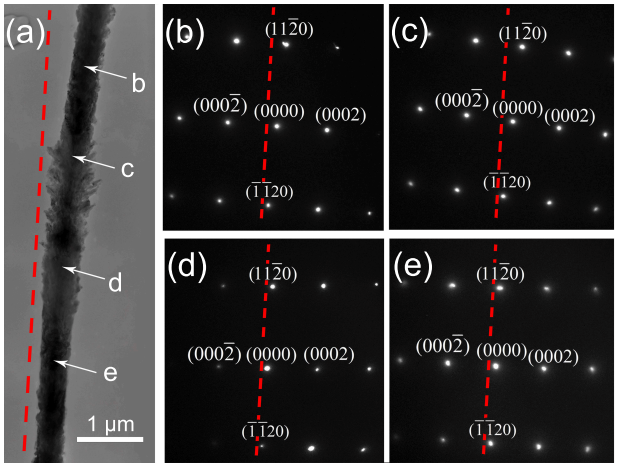

FIG. 2. TEM micrograph and electron diffraction patterns of a cobalt filament. The bright field image of the filament (a) and electron diffraction pattern (b-e) of the selected sites in (a) after correcting the magnetic rotation angle between the pattern and the bright field image. One may find that the single-crystalline diffraction patterns of (b)-(e) are essentially the same, except that they are rotated slightly due to the bending of the filament. The red dashed lines serve as a guide of eyes to show the slight deviation of the filament orientation at each site.

Figure 3 shows the MFM micrograph of the as grown cobalt filaments at remanence. The width of the filaments varies from 400nm to 800nm, and the height is in the range of 100nm - 250nm, which can be seen in the topography micrograph (Fig. 3(a)). MFM observations reveal two types of domains in the filaments. One possesses a zipper-like stray field pattern with the periodicity comparable to the filament width, which is denoted as pattern A in Fig. 3(b). The corresponding magnetic domain is cartooned in Fig. 3(c) (upper), and is termed as anti-parallel domain pattern (APDP). The other type of domains possesses a stripe-like stray field along the filament axis, marked as pattern B in Fig. 3(b). Four stripes with alternating dark and bright contrast can be identified. The magnetic domain is also schematically illustrated in Fig. 3(c) (lower), and is termed as compressed vortex domain pattern (CVDP). The magnetic domain with the stripe-like stray field has been studied before,[49]) and we will confirm our understanding of the domain later by simulation. In the same micrograph of Fig. 3(d), the brightness of CVDP is apparently weaker than that of APDP, suggesting that a weaker stray field exists for the case of CVDP.

The magnetic domain states shown in Fig. 3(b) are as-grown, which are not necessarily the ground state of the system. Therefore, we have applied an alternating external homogeneous in-plane magnetic field with a maximum amplitude of 0.2T and investigated the corresponding changes of the magnetic domain pattern. As illustrated in Fig. 3(d), although a few CVDPs remain unchanged, most of CVDPs transform to APDP, as indicated in the circled regions, suggesting that APDP is a more stable configuration. We have also applied a 0.6T magnetic field perpendicular to the plane of the filament arrays and slowly reduced the field back to zero. Remarkably, all the CVDPs in the filaments are changed to APDPs in the remanence state, as shown in Fig. 3(e). That is, a pure APDP is formed in the cobalt filaments. When these filaments are subsequently ac demagnetized in-plane, the APDP is found to be stable up to a 0.2 T demagnetization field, as shown in Fig. 3(f).

Our observations show that the type of magnetic domain after ac demagnetization depends on the local geometrical characters of the filaments. Figures 4(a)-4(c) show respectively the morphology of a filament, the height profile along the filament, and the corresponding MFM micrograph. One may find that the magnetic domain in the filament is sensitive to the height of the filament. The domain pattern evolves abruptly between APDP and CVDP depending on the filament thickness, as marked by the circle in Fig. 4(c). We also performed statistical analysis on the geometrical size of the filament and the type of magnetic domains, as shown in Fig. 4(d), where the black points stand for the observation of the sharp transition between CVDP and APDP. The red and blue points respectively represent the observation of CVDP and APDP states, respectively. This "phase diagram" demonstrates a clear dependence of the magnetic domain pattern on the geometrical characteristics of the filaments.

MFM images essentially represent the stray field distribution, which are determined by the spin texture in the filament. To verify our understanding, micromagnetic simulations were carried out using OOMMF[47] to simulate the spin configurations in the filaments. The geometrical parameters of the filament in the simulations, such as the shape and size, were selected based on MFM measurements. The filament possesses an in-plane uniaxial magneto-crystalline anisotropy perpendicular to the filament. Figure 5(a) illustrates the magnetic state of an 200nm-thick, 5m-long and 400nm-wide filament after relaxation from saturation. In the cross-sectional view, the magnetic domain curls to a round loop, forming a flat elliptical vortex pattern. The loop is uniform along the length of the filament. For comparison, Fig. 5(b) shows the state of a thinner filament, 100nm-thick, 5m-long and

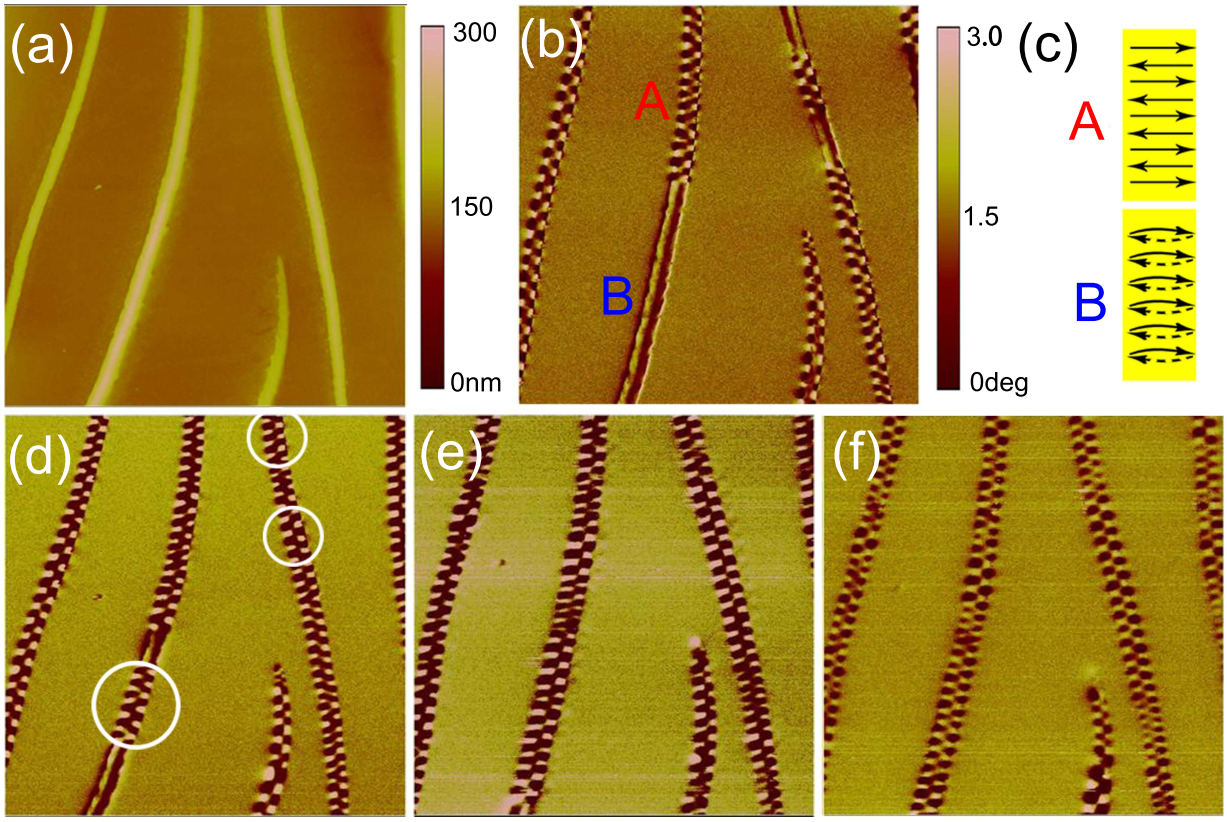

FIG. 3. AFM and MFM micrographs of the cobalt filaments. (a) The AFM topography of the filaments. (b) The magnetic domain patterns measured by MFM in the as-grown state. APDP and CVDP are labeled as A and B, respectively. (c) Schematic illustration of the magnetization configurations at site A and B in the filament, respectively. (d) The magnetic domain patterns observed after ac demagnetization with a maximum in-plane magnetic field of 0.2T at 1Hz. The circled region used to be CVDP, but changed to APDP after demagnetization. (e) The magnetic domain patterns at remanence after exposure to a 0.6 T magnetic field perpendicular to the plane, where all the CVDP has transformed into APDP. (f) The magnetic domain patterns of (e) after ac demagnetization. The APDP remains, although the spatial periodicity of the domain changes a bit. The size of the pictures is all 10μm*10μm. In MFM measurement the lift scan height was set as 100 nm in (b), (d)-(f).

400nm-wide. It follows that the magnetic moments are aligned perpendicular to the filament, and their directions alternate periodically, forming an anti-parallel domain pattern. The periodicity of the APDPs is about the width of the filament, consistent with the MFM results. It is noteworthy that blue and red colors in the plots represent the out of plane component of magnetization, which are related to the stray field (up and down) measured by MFM. The dark color stands for the scenario where the magnetization stays in-plane. The red and blue stripes along the z axis in Fig. 5(b) indicate the out-of-plane magnetization in domain walls. However, due to the fact that the width of domain walls is of the order of 10 nm and the resolution of MFM technique is roughly of the order of lift scan height (∼100 nm),[50] the stray field generated by domain walls can hardly be resolved by MFM experimentally. OOMMF simulations reproduce the experimentally observed MFM images.

It is interesting to identify the role of domain walls on the electric resistance by study the MR (defined as $((\rho(H)\text{-}\rho(H=0))/\rho(H=0))$ of the filaments with the specific magnetic domain patterns. In particular, the filament with periodic APDP provides a series of 180^o DWs, which can be applied to identify the effect of DWs on the transport properties. For the longitudinal, transverse, and perpendicular configurations, the magnetic field is applied along the long axis of the filament (the same as the direction of electrical current), in-plane and orthogonal to the filaments, and perpendicular to the plane of filament arrays, respectively. It turns out that the MR exhibits a dip in the longitudinal and perpendicular geometries, and a peak in the transverse geometry, as shown in Fig. 6(a). As that verified by MFM already, the remanence state in the perpendicular geometry is purely APDP. The perpendicular MR curves along decreasing and increasing field branches exhibit no hysteresis, indicating that the magnetization reversal process in an external magnetic field from APDP to the nearly saturated state is reversible. Due to the existence of CVDP, however, the longitudinal and transverse MR curves do exhibit hysteresis, as illustrated in the zoom-in view shown in Fig. 6(b). Figure 6(c) shows the top view of the gold

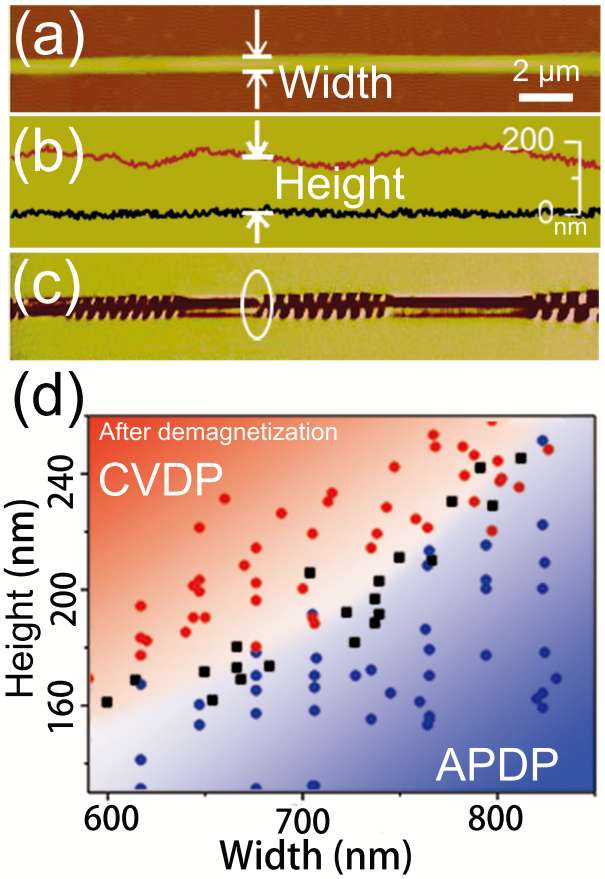

FIG. 4. Correlation of the magnetic domain patterns and geometrical profiles of the filaments. (a) The topography of a cobalt filament, where the filament width can be directly measured. (b) Height profile of the filament measured along the central axis of the filament. The red curve represents the height of the filament, and the dark curve is the height of nearby substrate. (c) MFM image of the filament after ac demagnetization in plane. In the region where the domain pattern changes abruptly, the width and height of the filament are recorded and plotted in d) as black dots. (d) The "phase diagram" for the appearance of different types of domains in the filament. It is confirmed that the filaments in the red region tend to possess CVDP while those in the blue region prefer to have APDP.

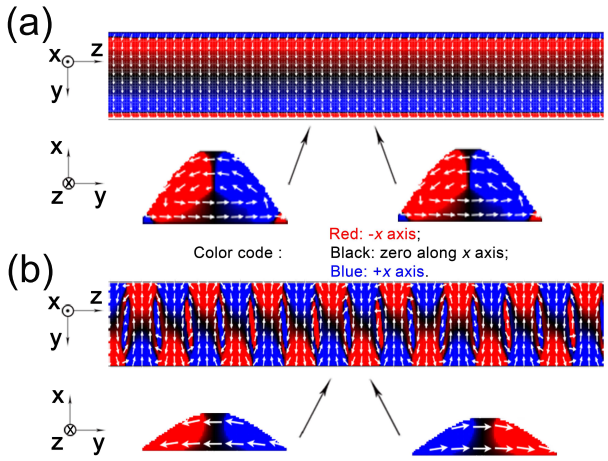

FIG. 5. The magnetic domains in a single-crystalline cobalt filament simulated by OOMMF. The geometrical parameters of the filament are 400nm-width, 200nm-height and 5μm-length in (a), and 400nm-width, 100nm-height and 5μm-length in (b). The white arrows represent the local spin direction. The out-of-plane spin components are color coded (components along $+x$ axis: Blue; $-x$ axis: red; zero: black). The cartoons under the plot of the filament in (a) and (b) show the magnetic domains obtained on the cross-section, as indicated by the arrows. The magnetic moments form a flattened vortex on the cross-sections shown in (a), and form an anti-parallel pattern in (b).

contacts to measure MR of the filaments. The MFM images of the filaments of the same area are demonstrated in Figs. 6(d) and 6(e). With Figs. 6(c)-(e) we are sure that in the region of MR measurements, there do exist the magnetic domains of APDP and CVDP in the initial magnetic state.

The DW contribution can be estimated from two marked points on the perpendicular and transverse MR in Fig. 6(a). As indicated by MFM measurements [Fig. 3(e)], when the applied magnetic field perpendicular to the sample plane is removed, a pure APDP state is obtained, as marked by the cyan circle on the perpendicular MR curve in Fig. 6(a). The other state is marked by the green circle on the transverse MR curve, where the magnetic field is approaching saturation, and all the moments should be nearly aligned in-plane but perpendicular to the filaments. The MR difference of these two states is about +0.15% of the resistance at zero-field $\rho(H = 0)$. Comparing these two states one may find that the resistance contributed by crystalline anisotropy within domains is nearly the same, and the MR difference originates from the series of DWs. We should point out that the magnetic field of 0.6T is approaching yet has not reached saturation in the transverse configuration. Yet we are not able to increase the field further due to the limitation of the maximum electric current in our home-made Helmholtz coils. We expect that when the saturation is reached, the MR effect from domain walls would be larger than +0.15%.

It has been reported that the magnetic domain configuration in a filament with circular cross-section depends on its diameter. When the diameter is below 150 nm, the magnetization orientation is reported to be sinusoidally modulated within the plane spanned by the wire axis and the c-axis,[51,52] whereas vortex magnetic domains appear in filaments with larger diameters.[24] Periodic APDP has also been observed in the initial magnetic state for filaments with circular diameter around 100 nm,[49,53] yet such a domain structure is unstable and vanishes after magnetization. However, the situation is quite different in our case, where the cross-section of the filament is a

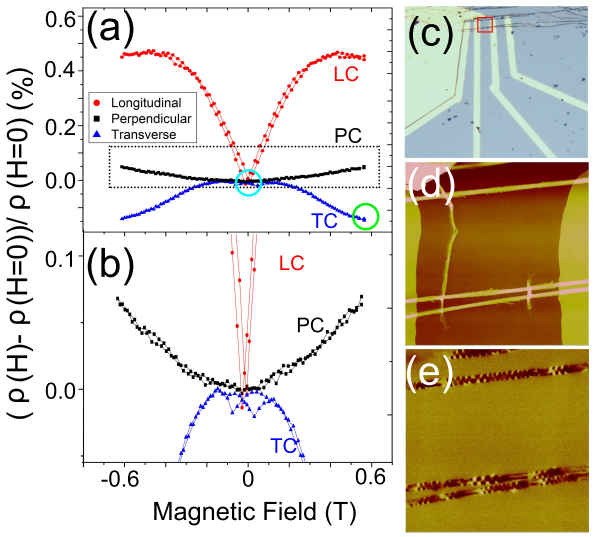

FIG. 6. (a) MR of the filament averaged over five cycles of magnetic field sweeping measured in longitudinal (LC), perpendicular (PC) and transverse (TC) configurations. The difference of MR in the cyan and the green circles is about 0.15% of the zero-field resistance $\rho(H = 0)$. (b) Zoom-in view of the dash-boxed region in (a). Note that the perpendicular MR shows little hysteresis, while longitudinal and transverse MR exhibit hysteretic behaviors near zero-field (H=0). (c) Top views of the gold contacts on Co filaments for MR measurements. (d) The topography of the three cobalt filaments between the gold contacts as labeled by the red box in (c). The vertical lines across the cobalt filaments are the residual photo-resist in making the contacts. (e) MFM image of (d), demonstrating the initial magnetic state of the filaments.

flat half-ellipse. For the filament with a flat cross-section, the periodic magnetic domain can be easily stabilized. This magnetization modulation is due to the competition between the crystalline anisotropy energy, the exchange energy and the demagnetization energy.[47,51] The total energy of a magnetic system can be expressed as

$$E = E_{ca} + E_{ex} + E_d$$
$$= \sum_i (K_1 sin^2\theta_i) - \sum_{ij} (\frac{A_{ij}\vec{M}_i \cdot \vec{M}_j}{\Delta_{ij}^2}) - \sum_i (\frac{\mu_0}{2}\vec{H}_d \cdot \vec{M}_i)$$

where K_1 is the magneto-crystalline anisotropy constant, θ_i is the angle between the magnetization and the easy magnetization axis of the filament; A_{ij} is an exchange constant, $\vec{M}_i$ represents the magnetization, Δ_{ij} denotes the distance between two magnetizations; μ_0 is the free-space permeability, $\vec{H}_d = -\mathbf{N} \cdot \vec{M}$ defines the demagnetization field and $\mathbf{N}$ is the demagnetization factor (tensor). Based on this equation, we can qualitatively compare the magnetic energy of APDP and CVDP as follows. Note that the easy axis of the cobalt filaments is along the c-axis, i.e., in the sample plane and perpendicular to the filament. Since CVDP possesses the magnetization components perpendicular to c-axis in order to form a loop, according to the first term of the equation, CVDP has higher magneto-crystalline anisotropy energy. In contrast, for APDP, all the magnetizations are either parallel or anti-parallel to the c-axis, so the magneto-crystalline anisotropy energy vanishes. Concerning the exchange energy, for CVDP, topologically on each cross-section of the filament, the magnetization forms a closed flat loop, indicating that on top and bottom portions of the filament cross-section, the magnetic moments are anti-parallel. Since the thickness of the cobalt filament is on the order of 200 nm, according to the second term of the equation, the small separation between the top and bottom surfaces of the CVDP region makes the exchange energy large. For APDP, the exchange energy of anti-parallel magnetizations of the neighboring domains, which is separated by an average distance of about 400 nm, turns out to be smaller than that of CVDP. For this reason, we expect that here the exchange energy in CVDP will be higher than that of APDP. The third term of the equation is contributed by demagnetization. For a thin, flat structure, the aspect ratio σ is small, so the demagnetization factor $N_\perp$ perpendicular to the sample plane is rather large. If the magnetization possesses a perpendicular component with respect to the sample plane, the demagnetization energy will consequently be large. For this reason, CVDP, which is featured by the flat vortex magnetization, results in a larger demagnetization energy comparing to that of APDP, where the magnetization is anti-parallel between the neighboring domains and is all confined in the plane. The alignment of magnetizations in APDP reduces the demagnetization energy, despite that such an alignment will slightly increase the exchange energy by forming more domain walls. Based on these discussions, we expect that the total energy of CVDP is higher than that of APDP for smaller σ.

Anti-parallel domains structure has previously been observed in long stripes with easy axis perpendicular to the long axis of stripes.[32–34] Instead of understanding the domain configuration at remanence from the point of view of global energy, people may expect that the system can reach local energy minima.[54] In other wards, dynamics may play a role in the formation of anti-parallel magnetic domain pattern. To verify this mechanism requires time-resolved capability in characterizing the magnetic structures.

IV. CONCLUSIONS

Nowadays modern lithography has reached unprecedented precision in fabricating nanostructures, yet the cost and productivity remain to be the limiting factors. Self-assembly, in contrast, relies on inexpensive chemical processes and can be easily controlled. Although it usually lacks the precise positioning over large areas comparing to that of conventional lithography, it allows tuning of many chemical/physical parameters to optimize the filament morphology and structures, and hence to

achieve the desired domain patterns. In this paper we have demonstrated the transition of periodically antiparallel magnetic domains and compressed vortex domains in single-crystalline cobalt filaments depending on the geometrical parameters of the filaments. The antiparallel domains pattern is robust against demagnetization for filaments with smaller aspect ratios, and the pattern can be realized over the entire filament at remanence state by exposure to a saturation magnetic field perpendicular to the plane of the filament arrays. The magnetoresistance of a series of domain walls contributes to over 0.15% of the zero-field resistance $\rho(H = 0)$. It should be pointed out that the single-crystalline cobalt filaments shown here are self-organized by a wet electrochemical approach, which is scalable and cost-effective, and can be applied to the fabrication of other conductive magnetic nanowires. We expect it will be inspiring in searching for new structures/materials for spintronic memory and logic devices.

V. ACKNOWLEDGMENTS

This work was supported by grants from the State Key Program for Basic Research from MOST of China (Grant No. 2010CB630705 and 2012CB921502), and the NSF of China (Grant Nos. 11204127, 11034005, 11328402 and 61077023). The work at UCD was supported by the NSF (ECCS-1232275 and DMR-1543582).

* Corresponding author: muwang@nju.edu.cn

[1] E. Pop, Nano Res. **3**, 147 (2010).
[2] C. Chappert, A. Fert, and F. N. Van Dau, Nat. Mater. **6**, 813 (2007).
[3] A. Fert, Rev. Mod. Phys. **80**, 1517 (2008).
[4] D. D. Awschalom and M. E. Flatt, Nat. Phys. **3**, 153 (2007).
[5] S. S. P. Parkin, M. Hayashi, and L. Thomas, **320**, 190 (2008).
[6] S. Parkin and S. H. Yang, Nat. Nanotech. **10**, 195 (2015).
[7] D. A. Allwood, G. Xiong, C. C. Faulkner, D. Atkinson, D. Petit, and R. P. Cowburn, Science **309**, 1688 (2005).
[8] A. Brataas, A. D. Kent, and H. Ohno, Nat. Mater. **11**, 372 (2012).
[9] D. Chiba, G. Yamada, T. Koyama, K. Ueda, H. Tanigawa, S. Fukami, T. Suzuki, N. Ohshima, N. Ishiwata, Y. Nakatani, and T. Ono, Appl. Phys. Express **3**, 073004 (2010).
[10] I. M. Miron, T. Moore, H. Szambolics, L. D. Buda-Prejbeanu, S. Auffret, B. Rodmacq, S. Pizzini, J. Vogel, M. Bonfim, A. Schuhl, and G. Gaudin, Nat. Mater. **10**, 419 (2011).
[11] S. H. Yang, K. S. Ryu, and S. Parkin, Nat. Nanotech. **10**, 221 (2015).
[12] K.-S. Ryu, L. Thomas, S.-H. Yang, and S. Parkin, Nat. Nano. **8**, 527 (2013).
[13] S. Emori, U. Bauer, S.-M. Ahn, E. Martinez, and G. S. D. Beach, Nat. Mater. **12**, 611 (2013).
[14] G. Chen, T. Ma, A. T. NDiaye, H. Kwon, C. Won, Y. Wu, and A. K. Schmid, Nat. Commun. **4**, 2671 (2013).
[15] D. A. Gilbert, B. B. Maranville, A. L. Balk, B. J. Kirby, P. Fischer, D. T. Pierce, J. Unguris, J. A. Borchers, and K. Liu, Nat. Commun. **6**, 8462 (2015).
[16] R. Lavrijsen, J.-H. Lee, A. Fernandez-Pacheco, D. C. M. C. Petit, R. Mansell, and R. P. Cowburn, Nature **493**, 647 (2013).
[17] A. Fernandez-Pacheco, L. Serrano-Ramon, J. M. Michalik, M. R. Ibarra, J. M. De Teresa, L. OBrien, D. Petit, J. Lee, and R. P. Cowburn, Sci. Rep. **3**, 1492 (2013).
[18] L. Serrano-Ramon, A. Fernandez-Pacheco, R. Cordoba, C. Magen, L. A Rodriguez, D. Petit, R. P. Cowburn, M. R. Ibarra and J. M. De Teresa, Nanotechnology **24**, 345703 (2013).
[19] J. I. Martin, J. Nogues, K. Liu, J. L. Vicent, and I. K. Schuller, J. Magn. Magn. Mater. **256**, 449 (2003).
[20] Y. P. Ivanov, O. Iglesias-Freire, E. V. Pustovalov, O. Chubykalo-Fesenko, and A. Asenjo, Phys. Rev. B **87**, 184410 (2013).
[21] C. Feuillet-Palma, T. Delattre, P. Morfin, J. M. Berroir, G. Feve, D. C. Glattli, B. Placais, A. Cottet, and T. Kontos, Phys. Rev. B **81**, 115414 (2010).
[22] S. Da Col, S. Jamet, N. Rougemaille, A. Locatelli, T. O. Mentes, B. S. Burgos, R. Afid, M. Darques, L. Cagnon, J. C. Toussaint and O. Fruchart, Phys. Rev. B **89**, 180405(R) (2014)
[23] L. G. Vivas, M. Vazquez, J. Escrig, S. Allende, D. Altbir, D. C. Leitao, and J. P. Araujo, Phys. Rev. B **85**, 035439 (2012).
[24] Y. P. Ivanov, L. G. Vivas, A. Asenjo, A. Chuvilin, O. Chubykalo-Fesenko, and M. Vzquez, Europhys. Lett. **102**, 17009 (2013).
[25] M. A. Basith, S. McVitie, D. McGrouther, J. N. Chapman, and J. M. R. Weaver, J. Appl. Phys. **110**, 083904 (2011).
[26] S. Ikeda, K. Miura, H. Yamamoto, K. Mizunuma, H. D. Gan, M. Endo, S. Kanai, J. Hayakawa, F. Matsukura, and H. Ohno, Nat. Mater. **9**, 721 (2010).
[27] M. Gavagnin, , H. D. Wanzenboeck, D. Belic, and E. Bertagnolli, ACS Nano **7**, 777 (2012).
[28] P. P. J. Haazen, E. Mur, J. H. Franken, R. Lavrijsen, H. J. M. Swagten, and B. Koopmans, Nat. Mater. **12**, 299 (2013).
[29] T. Kamionka, M. Martens, K. W. Chou, M. Curcic, A. Drews, G. Schutz, T. Tyliszczak, H. Stoll, B. Van Waeyenberge, and G. Meier, Phys. Rev. Lett. **105**, 137204 (2010).
[30] X. M. Kou, X. Fan, R. K. Dumas, Q. Lu, Y. P. Zhang, H. Zhu, X. K. Zhang, Kai Liu, and J. Q. Xiao, Adv. Mater. **23**, 1393 (2011).
[31] R. Streubel, J. Lee, D. Makarov, M. Y. Im, D. Karnaushenko, L. Han , R. Sch?fer , P. Fischer , S. K. Kim, and O. G. Schmidt, Adv. Mater. **26**, 316 (2014).
[32] U. Ruediger, J. Yu, S. Zhang, A. D. Kent, and S. S. P. Parkin, Phys. Rev. Lett. **80**, 5639 (1998).
[33] T. Kohda, Y. Otani, V. Novosad and K. Fukamichi, IEEE Trans. Magn. **35**, 3472 (1999).
[34] J.-Y. Chauleau, B. J. McMorran, R. Belkhou, N. Bergeard, T. O. Mentes, M.A. Nino, A. Locatelli, J. Unguris, S. Ro-

hart, J. Miltat and A. Thiaville, Phys. Rev. B **84**, 094416 (2011)
[35] S. P. Dash, S. Sharma, R. S. Patel, M. P. de Jong, and R. Jansen, Nature **462**, 491 (2009).
[36] V. Garcia, , M. Bibes, L. Bocher, S. Valencia, F. Kronast, A. Crassous, X. Moya, S. Enouz-Vedrenne, A. Gloter, D. Imhoff, C. Deranlot, N. D. Mathur, S. Fusil, K. Bouzehouane, and A. Barthlmy, Science **327**, 1106 (2010).
[37] Z. Liu, P. C. Chang, C. C. Chang, E. Galaktionov, G. Bergmann, and J. G. Lu, Adv. Func. Mater. **18**, 1573 (2008).
[38] J. Li, F. Chen, F. Yu, C. Meng and M. wang, to be published.
[39] M. Wang, S. Zhong, X. B. Yin, J. M. Zhu, R. W. Peng, Y. Wang, K. Q. Zhang, and N. B. Ming, Phys. Rev. Lett. **86**, 3827 (2001).
[40] S. Zhong, Y. Wang, M. Wang, M. Z. Zhang, X. B. Yin, R. W. Peng, and N. B. Ming, Phy. Rev. E **67**, 061601 (2003).
[41] X. P. Huang, Z. L. Shi, M. Wang, M. Konoto, H. S. Zhou, G. B. Ma, D. Wu, R. W. Peng, and N. B. Ming, Adv. Mater. **22**, 2711 (2010).
[42] Y. Y. Weng, J. W. Si, W. T. Gao, Z. Wu, M. Wang,R. W. Peng, and N. B. Ming, Phys. Rev. E **73**, 051601 (2006).
[43] Y. Y. Weng, B. Zhang, S. J. Fu, M. Wang, R. W. Peng, G. B. Ma, D. J. Shu, and N. B. Ming, Phy. Rev. E **81**, 051607 (2010).
[44] M. Z. Zhang, S. Lenhert, M. Wang, L. F. Chi, N. Lu, H. Fuchs, and N. B. Ming, Adv. Mater. **16**,409 (2004).
[45] B. Zhang, Y. Y. Weng, X. P. Huang, M. Wang, R. W. Peng, N. B. Ming, B. J. Yang, N. Lu, and L. F. Chi, Adv. Mater. **21**, 3576 (2009).
[46] M. G. Freire, A. F. M. Claudio, J. M. Araujo, J. A. Coutinho, I. M. Marrucho, J. N. C. Lopes, and L. P. N. Rebelo, Chem. Soc. Rev. **41**, 4966 (2012).
[47] G. M. J. Donahue and D. G. Porter , NISTIR 6376 (1999); http://math.nist.gov/oommf.
[48] R. Ferre, K. Ounadjela, J. M. George, L. Piraux, and S. Dubois, Phys. Rev. B **56**, 14066 (1997).
[49] Y. Henry, K. Ounadjela, L. Piraux, S. Dubois, J. M. George, and J. L. Duvail, Eur. Phys. J. B **20**,35 (2001).
[50] M.R. Koblischkaa, U. Hartmanna, and T. Sulzbach, J. Magn. Magn. Mater. **272**, 2138 (2004).
[51] G. Bergmann, J. G. Lu, Y. Tao, and R. S. Thompson, Phys. Rev. B **77**, 054415 (2008).
[52] D. Kaur, S. Chaudhary, and D. K. Pandya, J. Appl. Phys. **114**, 043909 (2013).
[53] K. M. Lebecki and M. J. Donahue, Phys. Rev. B **82**, 096401 (2010).
[54] G. Leaf, H. Kaper, M. Yan, V. Novosad, P. Vavassori, R. E. Camley and M. Grimsditch, Phys. Rev. Lett. **96**, 017201 (2006).